

## Article

# Magnetic, Optical, and Thermic Properties of SrLnCuSe<sub>3</sub> (Ln = Dy, Ho, Er, Tm) Compounds

Navruzbek N. Habibullayev <sup>1,\*</sup>, Nikolay G. Naumov <sup>2</sup>, Alexander N. Lavrov <sup>2</sup>, Natalia V. Kuratieva <sup>2</sup>, Aleksandr S. Aleksandrovsky <sup>3,4</sup>, Aleksandr S. Oreshonkov <sup>3,4</sup>, Maxim S. Molokeev <sup>5,6,7</sup>, Irina V. Palamarchuk <sup>1</sup>, Ilya O. Yurev <sup>1,8</sup>, Yuriy G. Denisenko <sup>1,9</sup>, Oleg V. Andreev <sup>1,10</sup> and Alena D. Zakharova <sup>1</sup>

- <sup>1</sup> Institute of Chemistry, University of Tyumen, 625003 Tyumen, Russia; i.v.palamarchuk@utmn.ru (I.V.P.); i.o.yurev@utmn.ru (I.O.Y.); yu.g.denisenko@gmail.com (Y.G.D.); o.v.andreev@utmn.ru (O.V.A.); a.d.zakharova@utmn.ru (A.D.Z.)
- <sup>2</sup> Nikolaev Institute of Inorganic Chemistry SB RAS, 630090 Novosibirsk, Russia; naumov@niic.nsc.ru (N.G.N.); lavrov@niic.nsc.ru (A.N.L.); kuratieva@gmail.com (N.V.K.)
- <sup>3</sup> Kirensky Institute of Physics, Federal Research Center, KSC, SB RAS, 660036 Krasnoyarsk, Russia; aleksandrovsky@kirensky.ru (A.S.A.); oreshonkov@iph.krasn.ru (A.S.O.)
- <sup>4</sup> Department of Photonics and Laser Technology, Siberian Federal University, 660036 Krasnoyarsk, Russia
- <sup>5</sup> Laboratory of Crystal Physics, Kirensky Institute of Physics, Federal Research Center, KSC, SB RAS, 660036 Krasnoyarsk, Russia; msmolokeev@mail.ru
- <sup>6</sup> Laboratory of Theory and Optimization of Chemical and Technological Processes, University of Tyumen, 625003 Tyumen, Russia
- <sup>7</sup> Department of Physics, Far Eastern State Transport University, 680021 Khabarovsk, Russia
- <sup>8</sup> Department of Physical and Applied Chemistry, Kurgan State University, 640020 Kurgan, Russia
- <sup>9</sup> Department of General and Special Chemistry, Industrial University of Tyumen, 625000 Tyumen, Russia
- <sup>10</sup> Institute of Solid State Chemistry, UB RAS, 620990 Ekaterinburg, Russia
- \* Correspondence: habibullayev\_navruzbek@mail.ru



**Citation:** Habibullayev, N.N.; Naumov, N.G.; Lavrov, A.N.; Kuratieva, N.V.; Aleksandrovsky, A.S.; Oreshonkov, A.S.; Molokeev, M.S.; Palamarchuk, I.V.; Yurev, I.O.; Denisenko, Y.G.; et al. Magnetic, Optical, and Thermic Properties of SrLnCuSe<sub>3</sub> (Ln = Dy, Ho, Er, Tm) Compounds. *Magnetochemistry* **2023**, *9*, 194. <https://doi.org/10.3390/magnetochemistry9080194>

Academic Editors: José Martínez-Lillo and Boris Tsukerblat

Received: 8 June 2023

Revised: 20 July 2023

Accepted: 27 July 2023

Published: 29 July 2023



**Copyright:** © 2023 by the authors. Licensee MDPI, Basel, Switzerland. This article is an open access article distributed under the terms and conditions of the Creative Commons Attribution (CC BY) license (<https://creativecommons.org/licenses/by/4.0/>).

**Abstract:** SrLnCuSe<sub>3</sub> (Ln = Dy, Ho, Er, Tm) compounds crystallize in the *Pnma* and *Cmcm* orthorhombic space group and belong to the Eu<sub>2</sub>CuS<sub>3</sub> and KCuZrS<sub>3</sub> structural type, respectively. According to a single-crystal XRD study, the SrTmCuSe<sub>3</sub> unit cell parameters are  $a = 4.0631$  (4),  $b = 13.4544$  (14),  $c = 10.4430$  (10), and  $V = 570.88$  (10)<sup>3</sup>. All the studied SrLnCuSe<sub>3</sub> samples in the temperature range of 1.77–300 K demonstrate paramagnetic behavior without any features pointing to magnetic ordering. The measured Curie constants coincide with the values expected for Ln<sup>3+</sup> ions with good accuracy, which confirms the stoichiometric composition of the samples and the non-magnetic state of the copper ions, Cu<sup>1+</sup> ( $S = 0$ ). The conducted optical absorption study showed that the polycrystalline SrLnCuSe<sub>3</sub> (Ln = Dy, Ho, Er, Tm) samples are semiconductors with a direct bandgap ranging from 2.14 eV to 2.31 eV. Two indirect bandgaps were revealed and explained by the presence of optical transitions to highly dispersive subbands in the conduction band. The compounds demonstrate two reversible phase transitions  $\alpha \rightleftharpoons \beta$ ,  $\beta \rightleftharpoons \gamma$  and an incongruent melting at 1606 K (Dy), 1584 K (Ho), 1634 K (Er), and 1620 K (Tm) associated with the formation of solid solutions of SrSe, Cu<sub>2- $\chi$</sub> Se, and Ln<sub>2</sub>Se<sub>3</sub> binary compounds.

**Keywords:** single-crystal X-ray diffraction; Curie–Weiss dependence; magnetic susceptibility; effective magnetic momentum; bandgap; DFT calculations; Raman spectrometry; thermal analysis; scanning electron microscope

## 1. Introduction

SrLnCuSe<sub>3</sub> (Ln = La, Ce, Pr, Gd, Lu) compounds were first synthesized by Strobel and Schleid [1,2] and were shown to have an orthorhombic structure with three structural types (ST) and two space groups (SG) (Table 1). The SrLnCuSe<sub>3</sub> compounds are promising solar cell [3], magnetic [4–6], and thermoelectric [7,8] materials.

**Table 1.** Crystallographic data for SrLnCuSe<sub>3</sub> (Ln = La, Ce, Pr, Gd, Lu).

Compound	ST	SG	a (Å)	b (Å)	c (Å)	Ref.	
SrLaCuSe <sub>3</sub>	PbCuLaS <sub>3</sub>	<i>Pnma</i>	8.4882 (5)	4.2304 (3)	16.7123 (9)	[1]	
SrCeCuSe <sub>3</sub>			8.4613 (5)	4.2169 (2)	16.6342 (9)	[2]	
SrPrCuSe <sub>3</sub>	Eu <sub>2</sub> CuS <sub>3</sub>		10.9732 (6)	4.1651 (2)	13.4964 (8)	[2]	
SrGdCuSe <sub>3</sub>			10.6810 (7)	4.1079 (3)	13.4921 (8)	[1]	
SrLuCuSe <sub>3</sub>	KCuZrS <sub>3</sub>		<i>Cmcm</i>	10.4019 (7)	4.0498 (3)	13.4567 (8)	[1]

The EuLnCuS<sub>3</sub> and EuLnCuSe<sub>3</sub> compounds are nonmetallic magnetic materials with a Curie temperature ranging from 3.4 K to 6 K [4,5,9,10] (Table 2). The EuErCuSe<sub>3</sub> compound exhibits a ferrimagnetic phase transition at T<sub>c</sub> = 4.7 K [4]. The magnetic moments of rare-earth ions Eu<sup>2+</sup> (7.94 μB) and Er<sup>3+</sup> (9.59 μB) [4,11] form two magnetic sublattices with a mutual antiferromagnetic orientation and uncompensated total magnetic moment. For EuLnCuSe<sub>3</sub> (Ln = Sm, Tb, Dy, Ho, Tm, Yb), the relative deviations of the calculated magnetic moments from the experimental ones do not exceed 3%. For example, the experimental effective magnetic moment for EuTmCuSe<sub>3</sub> is 10.99 μB, while its calculated value is 10.962 μB. As for the corresponding Curie constants, the deviation is twice as large due to the quadratic dependence with respect to the values of effective magnetic moments [5]. SrNdCuS<sub>3</sub> and SrTmCuS<sub>3</sub> are paramagnetic at 296 K [12]. The experimental effective magnetic moment is equal to 3.611 μB and 7.378 μB for complex Nd and Tm sulfides, respectively. The calculated effective magnetic moments of Nd<sup>3+</sup> and Tm<sup>3+</sup> ions (3.618 μB and 7.561 μB, respectively) coincide well enough with their experimental values, thus confirming that the Sr<sup>2+</sup> ions exist in a non-magnetic state [12]. The influence of Ln<sup>3+</sup> and Cu<sup>+</sup> cations on the magnetic properties of SrLnCuSe<sub>3</sub> compounds can be traced by replacing the magnetic cation Eu<sup>2+</sup> (4f<sup>7</sup> 5d<sup>0</sup> 6s<sup>0</sup>) in the series of complex selenide compounds with a non-magnetic cation Sr<sup>2+</sup> (5s<sup>0</sup>). The magnetic properties of SrLnCuSe<sub>3</sub> compounds have never been studied before.

**Table 2.** Curie temperatures of some of EuLnCuS<sub>3</sub> and EuLnCuSe<sub>3</sub> compounds.

Compound	T <sub>c</sub> (K)	Type	Ref.
EuTbCuSe <sub>3</sub>	6.0	ferrimagnetic	[5]
EuDyCuSe <sub>3</sub>	5.5	ferrimagnetic	[5]
EuHoCuSe <sub>3</sub>	6.2	ferrimagnetic	[5]
EuErCuSe <sub>3</sub>	4.7	ferrimagnetic	[4]
EuTmCuSe <sub>3</sub>	4.5	ferrimagnetic	[5]
EuEuCuS <sub>3</sub>	3.4	ferromagnetic	[10]
EuGdCuS <sub>3</sub>	5.4	ferrimagnetic	[9]
EuTbCuS <sub>3</sub>	4.9	ferrimagnetic	[9]
EuDyCuS <sub>3</sub>	4.6	ferrimagnetic	[9]
EuTmCuS <sub>3</sub>	4.8	ferrimagnetic	[9]

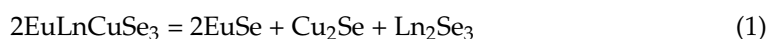
The optical bandgap was determined for the following series of compounds: EuLnCuSe<sub>3</sub> [4,5] and SrLnCuS<sub>3</sub> [12]. These compounds are wide-bandgap semiconductors [13] with ΔE<sub>g</sub> ranging from 1.58 eV to 2.45 eV. For EuLnCuSe<sub>3</sub>, the experimental ΔE<sub>g</sub> values were 1.58 eV (Nd, Sm), 1.72 eV (Gd), 1.79 eV (Er), 2.02 eV (Tm), and 2.1 eV (Lu) [4,5]. In all the series of these compounds, the ΔE<sub>g</sub> values increased with the increasing atomic number of lanthanide.

The electronic structure and the density of states of EuLnCuSe<sub>3</sub> (Ln = Ce, Ho, Yb) were determined by the DFT/B3LYP method [5,14]. The trajectory in the Brillouin zone passed

through the most symmetrical points of the orthorhombic  $Pnma$  structure. According to the calculations, the upper part of the valence band is formed by the ground states of selenium and copper, while the lower part of the band is formed by the states of rare earth elements (REE) and Eu ions [5,15].

In works [5,16], the Raman spectra of compounds  $BaLnCuS_3$  and  $EuLnCuSe_3$  were studied in detail. All members of the  $A^{II}LnCuX_3$  ( $A = Sr, Ba, Eu; X = S, Se$ ) family are formed by the layers of  $CuX_4$  tetrahedra and  $LnX_6$  octahedra. According to the lattice dynamics simulations, vibrations at low wavenumbers ( $20\text{--}115\text{ cm}^{-1}$ ) are related to the vibration of such layers. The strong bands at  $62$  and  $67\text{ cm}^{-1}$  in  $BaPrCuS_3$  and  $BaSmCuS_3$  are related to the antisymmetric displacements of structural layers.  $EuTbCuSe_3$  (ST  $Eu_2CuS_3$ , SG  $Pnma$ ) and  $EuTmCuSe_3$  (ST  $KZrCuS_3$ , SG  $Cmcm$ ) exhibit bands only in the region up to  $\sim 250\text{ cm}^{-1}$ . The experimental and calculated spectra of the latter two compounds are very similar, having the most intense bands at  $\sim 60$  and  $\sim 180\text{ cm}^{-1}$ . However, the calculated spectra of  $EuTbCuSe_3$  contain an additional clearly visible band at  $\sim 15\text{ cm}^{-1}$  and a less intense peak in the region  $40\text{--}45\text{ cm}^{-1}$ .

Thermal characteristics were determined for the  $SrLnCuS_3$  [17] and  $EuLnCuSe_3$  [4] series. When plotted as a function of the lanthanide radius  $r_{Ln^{+3}}$ , the temperatures of incongruent decomposition of the complex sulfides and selenides showed both similar and different regularities. The  $EuLnCuSe_3$  compounds for La, Ce, Pr, and Nd decompose according to the following solid-state reaction [4]:



Beginning with Gd, the compounds exhibit polymorphic phase transitions. The dependences of phase transition temperatures on  $r_{Ln^{+3}}$  manifest a tetrad effect. Since  $SrLnCuSe_3$  compounds with yttrium subgroup lanthanides are expected to be thermally stable, studying their properties is a relevant task. We have found no information on the optical, magnetic, and thermal properties of  $SrLnCuSe_3$  ( $Ln = Dy, Ho, Er, Tm$ ) compounds. Thus, in the present work, samples of  $SrLnCuSe_3$  compounds ( $Ln = Dy, Ho, Er, Tm$ ) were prepared, the structure of  $SrTmCuSe_3$  was established, and the optical, magnetic, and thermal properties of these compounds were determined.

## 2. Experimental Methods

### 2.1. Synthesis

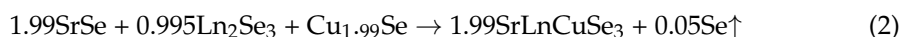
The following starting materials were used for the synthesis of a polycrystalline  $SrLnCuSe_3$  sample ( $Ln = Dy, Ho, Er, Tm$ ): dense samples of rare-earth metals Dy, Ho, Er, Tm (99.99 at.%) (TOPLUS, Ltd., Guangzhou, China), copper plate (99.99 at.% Cu), selenium granules (99.998 at.% Se), powdered strontium oxalate (99.98 at.%  $SrC_2O_4 \cdot nH_2O$ ), and argon (99.998 at.% Ar) (JSC Khimreaktiv, Yekaterinburg, Russia). Hydrogen (99.9999%) was obtained by the electrolysis of deionized  $H_2O$  on a Spektr generator (LLC SHC "Spektr" Dzerzhinsk, Russia).

The  $SrLnCuSe_3$  compounds were prepared from the  $Ln_2Se_3$ ,  $SrSe$ , and  $Cu_{1.99}Se$  metal selenides. The  $Ln_2Se_3$  samples were prepared from simple substances of chemical elements (a rare earth metal and selenium). The metals were crushed by drilling. The weighted samples with a total mass of 15 g were weighted with an accuracy of  $\pm 0.0001\text{ g}$  on a METLER TOLEDO ME 204 balance and placed in  $\sim 9\text{ cm}^3$  optical quartz ampoules [4]. The ampoules were evacuated to 0.1 Pa, sealed, and placed in a muffle furnace. The furnace temperature was raised to 1170 K at a rate of 50 K/day. The samples were kept at 1170 K for 500 h.

Copper semiselenide was prepared using simple copper and selenium substances taken in the 1.990 Cu:1.000 Se molar ratio. The weighted samples of the substances with a total mass of 30 g were also placed in a quartz ampoule, which was then evacuated and sealed. The ampoule was heated up to 1440 at a rate of 50 K/h. The melt was stirred several times and crystallized upon cooling at a rate of 50 K/h [18].

SrSe was prepared by treating a  $\text{SrC}_2\text{O}_4 \times n\text{H}_2\text{O}$  powder with a mass of 15 g by a flow of  $\text{H}_2\text{Se}$  that was supplied at a rate of 10 L/h at 1270 K for 2 h.  $\text{H}_2\text{Se}$  was prepared by  $\text{H}_2$  bubbling through melted selenium at 770 K.

The  $\text{SrLnCuSe}_3$  compounds were prepared from weighted samples of  $\text{Ln}_2\text{Se}_3$ , SrSe, and  $\text{Cu}_{1.99}\text{Se}$  metal selenides calculated so that the metal ratio in the samples was equal to Sr:Ln:Cu = 1:1:1 (Equation (2)). The metal selenide samples were ground in an agate mortar and placed in a graphite crucible inside a quartz ampoule. The ampoules were evacuated and sealed. The crucibles with the samples were heated to 1700 K in a high-frequency current setup. The samples were kept at this temperature for up to 3–5 min and then crystallized while the temperature was decreased to 1450 K. The heating–cooling cycles were repeated three times. The ampoules with the samples were annealed at 1170 K for 600 h.



The  $\text{SrTmCuSe}_3$  crystals were grown by the recrystallization of a polycrystalline sample in a CsCl melt at 1020 K. The  $\text{SrTmCuSe}_3$  crystals were obtained as a mixture with  $\text{CsTm}_2\text{Cu}_3\text{Se}_5$  crystals (ICSD#413681 [19] orthorhombic, SG *Cmcm*,  $a = 4.0970$  (3) Å,  $b = 14.6667$  (16) Å, and  $c = 17.1765$  (18) Å). These crystals for structural analysis from the crystallized melt were selected manually.

## 2.2. Analysis Methods

The structural and phase composition of the samples was determined by X-ray powder diffraction (XRPD) on a Philips X'PERT PRO MRD diffractometer using  $\text{CuK}_\alpha$  radiation in the  $2\theta$  range from 10 to  $130^\circ$  with a step of  $0.02^\circ$  [20]. The  $\text{SrGdCuSe}_3$  (ST  $\text{Eu}_2\text{CuS}_3$ ) and  $\text{SrLuCuSe}_3$  (ST  $\text{KZrCuS}_3$ ) [1] were taken as starting models for Rietveld refinement which was performed using TOPAS 4.2 [21].

The single-crystal XRD data for  $\text{SrTmCuSe}_3$  were collected using graphite monochromated  $\text{MoK}_\alpha$  radiation ( $\lambda = 0.71073$  Å) at 150 (2) K on an X8APEX Bruker Nonius diffractometer equipped with a 4K CCD area detector [22,23]. The intensities were measured using the  $\varphi$ -scanning technique. Absorption corrections were applied empirically using the SADABS program [24]. The structures were solved by direct methods of the difference Fourier synthesis and refined by the full-matrix least squares using the SHELXTL package [25,26]. Atomic thermal parameters were refined anisotropically.

Magnetization measurements were performed using a Quantum Design MPMS-XL SQUID magnetometer in the temperature range 1.77–300 K at magnetic fields up to 10 kOe [27,28]. In order to determine the paramagnetic component of the molar magnetic susceptibility,  $\chi_p(T)$ , the temperature-independent diamagnetic contribution,  $\chi_d$ , and a possible magnetization of ferromagnetic micro-impurities,  $\chi_{\text{FM}}(T)$ , were evaluated and subtracted from the measured values of the total molar susceptibility  $\chi = M/H$ . While  $\chi_d$  was calculated using Pascal's additive scheme,  $\chi_{\text{FM}}(T)$ , if any, was determined from the measured isothermal  $M(H)$  dependencies and  $M(T)$  data taken at different magnetic fields.

The thermal analysis of the compounds  $\text{SrHoCuSe}_3$  and  $\text{SrTmCuSe}_3$  was performed using the STA 449 F3 Jupiter instrument equipped with a (W3%Re–W25%Re) thermocouple in the He (99.999%, Russia) flow. The analyzed powder sample weighed  $(90\text{--}100) \pm 0.01$  mg in open graphite crucibles. In the temperature range where thermal events were observed the heating rate was 10 K/min. The results of the DSK/TG/t experiments were processed in the Proteus-6 programs package [29]. The thermal analysis of the  $\text{SrDyCuSe}_3$  and  $\text{SrErCuSe}_3$  was carried out on a SETARAM SETSYS Evolution analyzer with a PtRh-6%–PtRh-30% thermocouple. The 100 mg powder samples were placed in a 0.1 mL conical quartz ampoule, and the ampoule was evacuated and sealed. The heating was performed at a rate of 10 K/min in the temperature range where thermal events were observed. The DSC results were processed using the SETSOFT 2000 program [30].

The reflectance spectra were recorded on a Shimadzu UV-3600 spectrophotometer (Kyoto, Japan) using a powdered sample [31]. Raman spectra were measured on a LabRAM HR Evolution spectrometer (Horiba, Ltd., Kyoto, Japan) (He–Ne laser, 633 nm).

The distribution of chemical elements in thin sections of the samples after thermal analysis was determined on a JEOL JSM-6510LV scanning electron microscope using an Oxford Instruments X-Max EDS microanalysis system [32]. The survey was performed at an accelerating voltage of 20 kV. The EDS data processing and the mapping were carried out using the AZtec program.

### 3. Results and Discussion

#### 3.1. The X-ray Powder Diffraction

The samples contained more than 95 wt.% of the main component ( $\text{SrLnCuSe}_3$ ); the representative  $\text{SrTmCuSe}_3$  XRPD pattern is shown in Figure 1. The diffraction data for the  $\text{SrDyCuSe}_3$  and  $\text{SrHoCuSe}_3$  compounds were identified in the orthorhombic system, the  $Pnma$  space group, and the  $\text{Eu}_2\text{CuS}_3$  structural type. The  $\text{SrErCuSe}_3$  and  $\text{SrTmCuSe}_3$  compounds were identified in the orthorhombic system, the  $Cmcm$  space group, and the  $\text{KCuZrS}_3$  structural type (Table 3). The XRPD structure parameters of  $\text{SrTmCuSe}_3$  are close to the ones obtained from a single crystal. Refinement was stable and gave low R-factors (Table 3 and Table S1 in the Supplementary Materials). The coordinates of the atoms and main bond lengths are in Tables S2 and S3 in the Supplementary Materials. Additional crystallographic details and structure refinements of the single-crystal XRD experiment for  $\text{SrTmCuSe}_3$  are summarized in Tables 4 and 5.

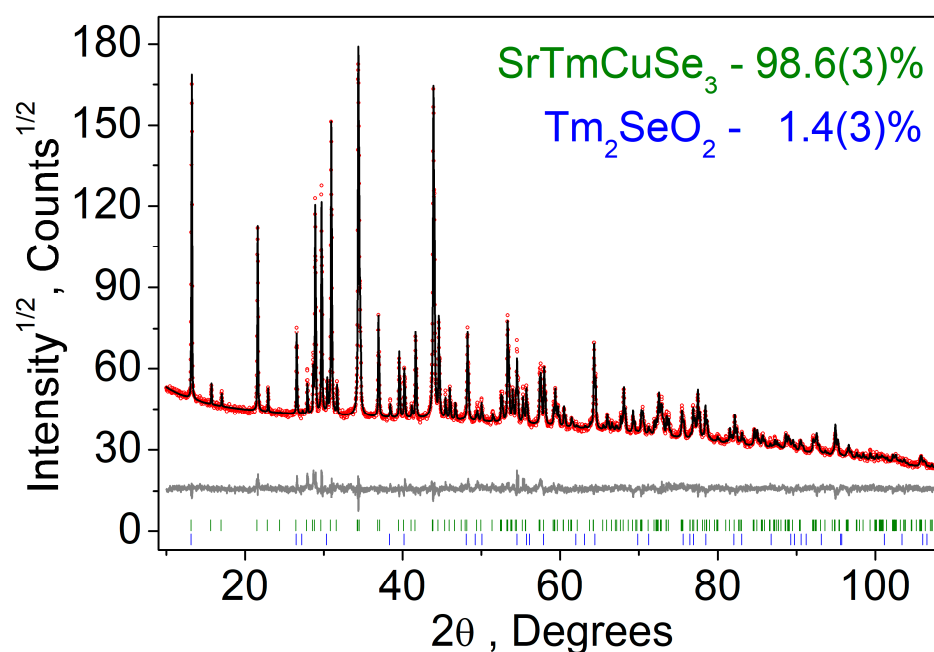


Figure 1. Difference Rietveld plot of  $\text{SrTmCuSe}_3$ .

Table 3. Unit cell parameters for  $\text{SrLnCuSe}_3$  (Ln = Dy, Ho, Er, Tm) compounds.

$\text{SrLnCuSe}_3$	ST	SG	a, (Å)	b, (Å)	c, (Å)	V (Å <sup>3</sup> )	R <sub>B</sub> , %
$\text{SrDyCuSe}_3$	$\text{Eu}_2\text{CuS}_3$	$Pnma$	10.5644 (5)	4.0871 (3)	13.4758(6)	581.86 (5)	5.10
$\text{SrHoCuSe}_3$			10.5335 (4)	4.08358 (17)	13.4749 (5)	579.61 (4)	5.90
$\text{SrErCuSe}_3$	$\text{KZrCuS}_3$	$Cmcm$	4.06942 (6)	13.4761 (2)	10.46463 (15)	573.881 (15)	2.80
$\text{SrTmCuSe}_3$			4.06935 (6)	13.4758 (2)	10.46441 (15)	573.844 (15)	2.56
$\text{SrTmCuSe}_3$ (X-ray)			4.0631 (4)	13.4544 (14)	10.4430 (10)	570.88 (10)	

**Table 4.** Crystal data and structure refinement for SrTmCuSe<sub>3</sub>.

Empirical formula	SrTmCuSe <sub>3</sub>
Formula weight	556.97
Temperature	293(2) K
Wavelength	0.71073 Å
Crystal system	Orthorhombic
Space group	<i>Cmcm</i>
Unit cell parameters	a = 4.0631 (4) Å b = 13.4544 (14) Å c = 10.4430 (10) Å
Volume	570.88 (10) Å <sup>3</sup>
Z	4
Density (calculated)	6.480 g/cm <sup>3</sup>
Absorption coefficient	47.372 mm <sup>-1</sup>
F(000)	952
Crystal size	0.170 × 0.100 × 0.070 mm <sup>3</sup>
Theta range for data collection	3.028–30.437°
Index ranges	−5 ≤ h ≤ 3, −18 ≤ k ≤ 18, −12 ≤ l ≤ 14
Reflections collected	2583
Independent reflections	508 [R(int) = 0.0366]
Completeness to theta = 25.25°	99.7%
Absorption correction	Semi-empirical from equivalents
Refinement method	Full-matrix MLS on F <sup>2</sup>
Data/restraints/parameters	508/0/24
Goodness-of-fit on F <sup>2</sup>	1.138
Final R indices [I > 2σ(I)]	R1 = 0.0188, wR2 = 0.0432
R indices (all data)	R1 = 0.0211, wR2 = 0.0438
Largest diff. peak and hole	1.716 and −1.641 e/Å <sup>3</sup>

**Table 5.** Positional atomic and displacement parameters for SrTmCuSe<sub>3</sub>.

Atom	Wyckoff	x	y	z	Occup.	U <sub>eq</sub> (Å <sup>2</sup> )
Sr (1)	4c	0	0.7508 (1)	0.25	1	0.012 (1)
Cu (1)	4c	0	0.4710 (1)	0.25	1	0.012 (1)
Tm (1)	4a	0	0	0	1	0.006 (1)
Se (1)	4c	0	0.0780 (1)	0.25	1	0.006 (1)
Se (2)	8f	0	0.3613 (1)	0.0626 (1)	1	0.007 (1)

The asymmetric unit of the structure of SrTmCuSe<sub>3</sub> contains one site for each strontium, thulium, and copper atom and two independent selenium sites (Figure 2a). The thulium atom in the special 4a (*2/m* symmetry) position is in a slightly distorted octahedral environment of sulfur atoms (Figure 2b). The copper atom in the special 4c (*m2m* symmetry) position is in a slightly distorted tetrahedral environment of selenium atoms (Figure 2c). TmSe<sub>6</sub> and CuSe<sub>4</sub> polyhedra form anionic chains consisting of slightly distorted {TmSe<sub>6</sub>} octahedra sharing edges along the (100) direction. Each chain is linked with two adjacent chains through {CuSe<sub>4</sub>} tetrahedra in which copper is linked with two selenium atoms

within one chain and with two selenium atoms from the adjacent chain so that negatively charged  $\{\text{TmCuSe}_3\}$  layers are formed (Figure S1 in the Supplementary Materials). The Sr atoms are located between these layers and have a bicapped trigonal prismatic environment of selenium. Table 6 presents selected interatomic distances for  $\text{SrTmCuSe}_3$ .

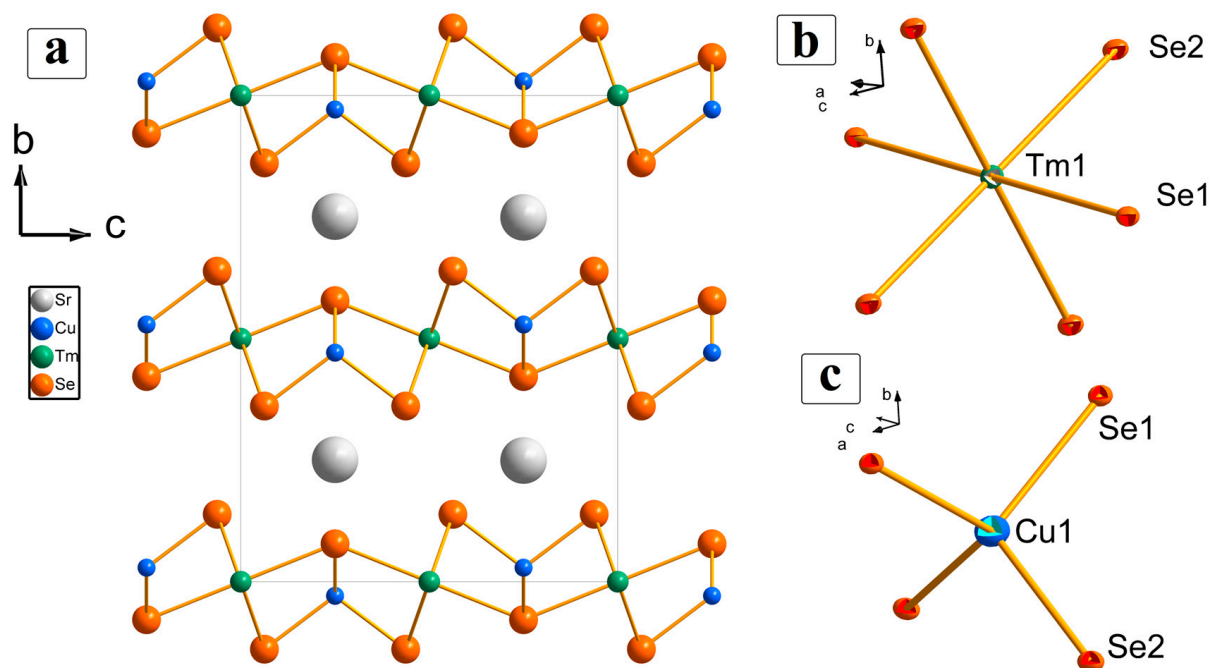


**Figure 2.** Crystal structure of  $\text{SrTmCuSe}_3$  (a),  $\text{Tm}^{3+}$  (b), and  $\text{Cu}^+$  (c) environment as viewed along the  $a$  axis.

**Table 6.** Selected interatomic distances ( $\text{\AA}$ ) for  $\text{SrTmCuSe}_3$ .

Bond	Bond Length, $\text{\AA}$
Cu-Se	$2.4513(9) \times 2$
	$2.4899(8) \times 2$
Mean	24706
Tm-Se	$2.8139(4)$
	$2.8140(4)$
	$2.8351(4) \times 2$
	$2.8350(4) \times 2$
Mean	2828
Sr-Se	$3.0870(9) \times 2$
	$3.1885(6) \times 4$
Mean	3265
Tm...Tm	In layer: $4.063 \times 2$
	$5.221 \times 2$
	$6.616 \times 4$
	Between layers: $7.027 \times 4$

### 3.2. Magnetic Measurements

The studied  $\text{SrLnCuSe}_3$  samples in the entire temperature range of 1.77–300 K exhibit paramagnetic behavior without manifestations of thermomagnetic irreversibility or features that could be associated with the formation of a static magnetic order (Figure 3A–D), in contrast to the Eu-containing analogs  $\text{EuLnCuSe}_3$  and  $\text{EuLnCuSe}_3$  [4,9]. For the  $\text{SrErCuSe}_3$  sample, for example, the temperature dependence of the magnetic susceptibility  $\chi_p$  can for-

ally be described quite well by the Curie–Weiss law  $\chi_p = C/(T - \theta)$ , with parameters  $C \approx 11.21$  emuK/mol and  $\theta \approx -5$  K (Figure 3A). The effective moment  $\mu_{\text{eff}} \approx (8C)^{1/2} \approx 9.47 \mu_B$  per formula unit, which corresponds to the obtained Curie constant  $C \approx 11.21$  emuK/mol, agrees pretty well with the value  $\mu_{\text{eff}}(\text{Er}^{3+}, \text{theor.}) \approx 9.59 \mu_B$  theoretically expected for  $\text{Er}^{3+}$  ( $S = 3/2$ ;  $L = 6$ ;  $J = 15/2$ ) ions and the typical empirical value  $\mu_{\text{eff}}(\text{Er}^{3+}, \text{empir.}) \approx 9.50 \mu_B$  observed in erbium compounds. This agreement clearly indicates that only erbium ions in  $\text{SrErCuSe}_3$  are magnetic, while copper ions adopt a non-magnetic state  $\text{Cu}^{1+}$  ( $S = 0$ ).

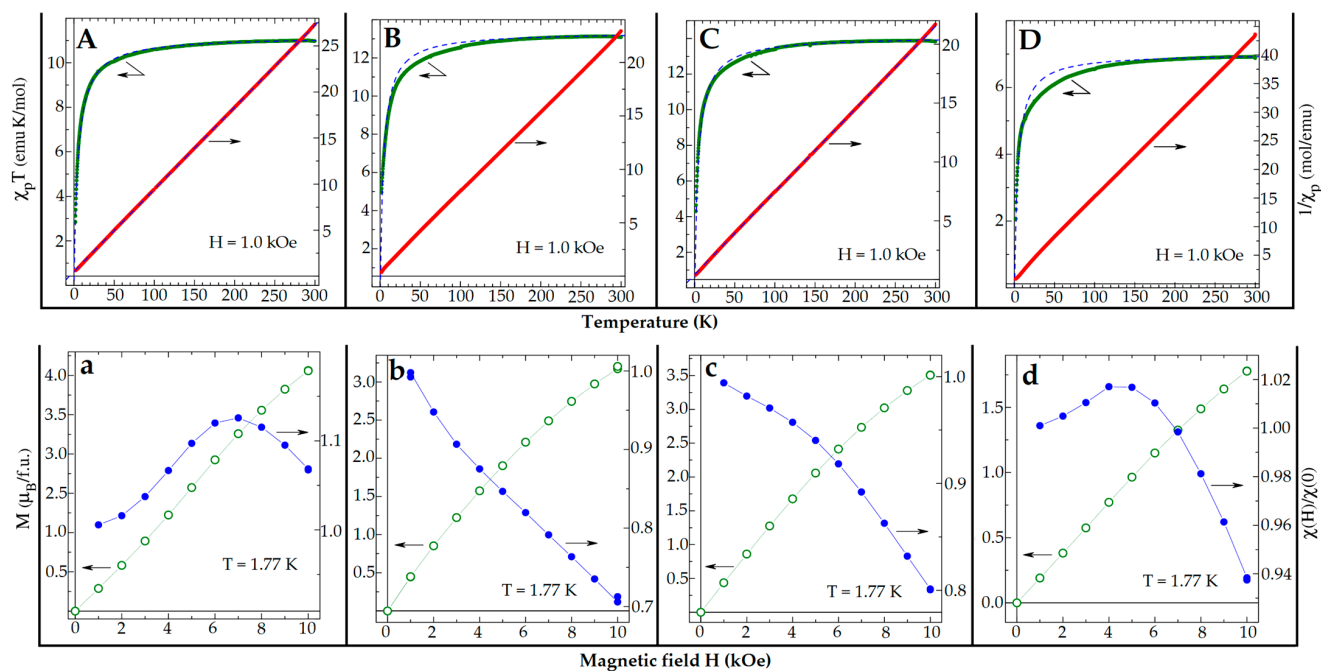
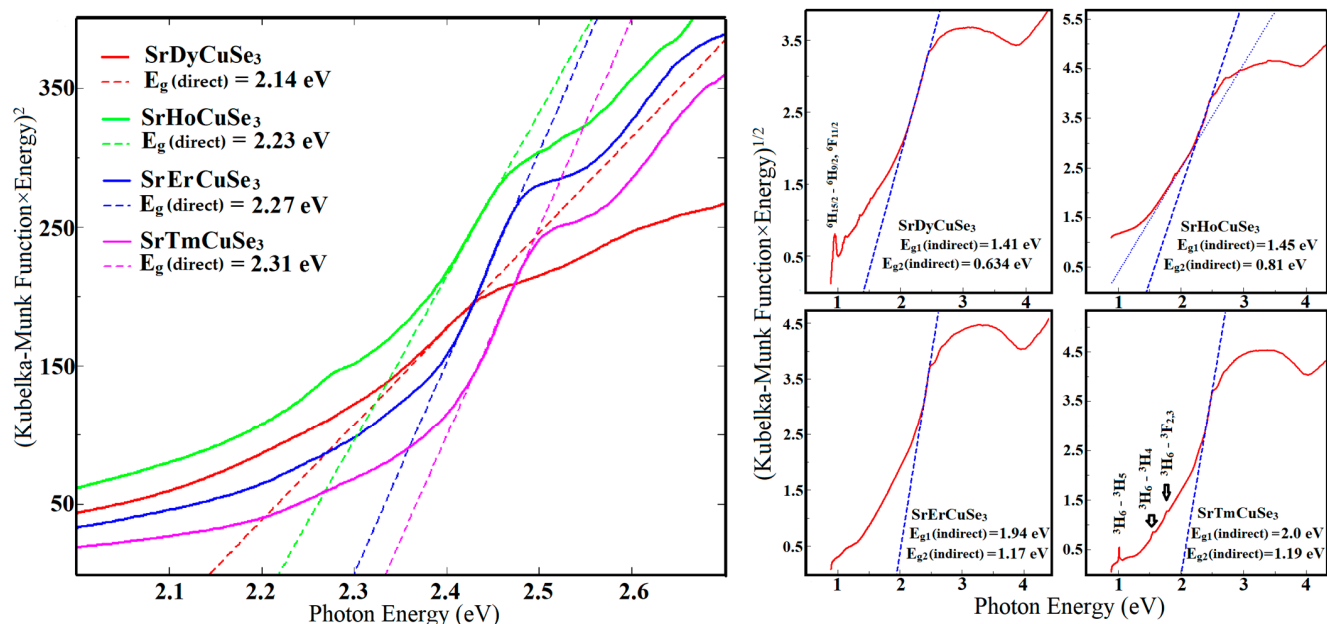


**Figure 3.** (A–D) Temperature dependences of  $\chi_p T$  and  $1/\chi_p$  measured for polycrystalline samples  $\text{SrErCuSe}_3$  (A),  $\text{SrDyCuSe}_3$  (B),  $\text{SrHoCuSe}_3$  (C), and  $\text{SrTmCuSe}_3$  (D) at the magnetic field  $H = 1$  kOe. The blue dashed lines illustrate the possibility of describing the experimental data by the Curie–Weiss dependence. (a–d) Field dependences of the magnetization  $M(H)$  and normalized magnetic susceptibility  $\chi(H)/\chi(0)$ , measured at  $T = 1.77$  K, for samples  $\text{SrErCuSe}_3$  (a),  $\text{SrDyCuSe}_3$  (b),  $\text{SrHoCuSe}_3$  (c), and  $\text{SrTmCuSe}_3$  (d).

The Weiss constant  $\theta \approx -5$  K, however, can by no means be directly taken as a characteristic of the magnetic interactions between  $\text{Er}^{3+}$  ions. Negative values of the Weiss constant and, accordingly, the decrease in  $\chi_p T$  with decreasing temperature (Figure 3A) may be associated with two factors: (i) crystal-field splitting of the ground-state  $^4I_{15/2}$  multiplet of  $\text{Er}^{3+}$  ions [33] and (ii) the antiferromagnetic (AF) interaction between  $\text{Er}^{3+}$  ions. Given that these two factors should cause different temperature dependences of  $\chi_p T$ , the observed relatively good agreement of  $\chi_p T$  data in  $\text{SrErCuSe}_3$  with the Curie–Weiss dependence seems to indicate a significant contribution of AF interactions. However, the analysis of the temperature dependence of  $\chi_p$  alone is insufficient for unambiguous conclusions. Additional information can be obtained from the field dependences of magnetization  $M(H)$  and normalized magnetic susceptibility  $\chi(H)/\chi(0)$ . While the measured  $M(H)$  curves are perfectly linear at high temperatures ( $\chi(H) = M(H)/H = \text{const}$ ), the magnetization is noticeably non-linear in the lowest temperature region. As can be seen in Figure 4a, as the magnetic field increases, the magnetic susceptibility at  $T = 1.77$  K initially grows, indicating the field suppression of AF correlations between  $\text{Er}^{3+}$  ions, and then decreases at  $H > 7$  kOe as expected for the conventional process of the magnetization of paramagnetic moments described by the Brillouin function. Thus, AF interactions between rare-earth ions are indeed present in  $\text{SrErCuSe}_3$  and are responsible for a substantial part of the  $\chi_p T$  decrease at low temperatures. The combined effect of the crystal-field splitting of  $\text{Er}^{3+}$  levels and

the AF interaction between the ions, however, brings about a relatively small constant  $\theta \approx -5$  K. The weak effect of the crystal-field splitting implies a rather high symmetry of the  $\text{Er}^{3+}$  ion environment in the crystal lattice, and the weakness of AF interactions indicates that the exchange coupling is virtually absent, leaving the  $\text{Er}^{3+}$  ions to interact only through the dipole–dipole mechanism.



it is clear that, owing to a fairly symmetric coordination,  $Tm^{3+}$  ions have not acquired a singlet ground state, which is often observed in compounds with  $Tm^{3+}$  ions in a strongly anisotropic environment [33]. In the case of the  $SrDyCuSe_3$  and  $SrHoCuSe_3$  compounds, the field dependences  $M(H)$  and  $\chi(H)/\chi(0)$  have a monotonic appearance, without significant features that could definitely be attributed to the magnetic-field suppression of AF interactions (Figure 3b,c). Nevertheless, in both compounds, the magnetization at  $H = 10$  kOe is only  $\approx 3.2$ – $3.5 \mu_B$  per  $Ln^{3+}$  ion, which is significantly reduced compared to free ions due to the splitting of their multiplet levels.

### 3.3. The Optical Properties

The Kubelka–Munk functions modified for the determination of either direct or indirect optical bandgaps are presented in Figure 4 and Figure S2 in the Supplementary Materials, while the experimental diffuse reflectance spectra are presented in Figure S3.

Figures 4 and S2 demonstrate that the shapes of all the Kubelka–Munk functions modified for direct bandgap are similar to each other. They all exhibit a band in the range of 2.5–4 eV that contains a moderate-height but well-pronounced linear region that must be associated with the fundamental absorption onset. To verify this, an enlarged region from 2 to 2.7 eV is presented in Figure 4. The linear region is rather weakly pronounced in Dy-selenide, but it becomes better pronounced in Ho-selenide and is even better seen in Er- and Tm-selenides. The regularity in the behavior of the linear region in the range from 2 to 2.7 eV indicates that this feature is due to an interband transition. The Kubelka–Munk function of all four crystals under study contains another band at an energy higher than 4 eV. This band is due to the transitions between electronic bands lower than the top of the valence band and/or higher than the bottom of the conduction band. All the Kubelka–Munk functions modified for indirect bandgaps are similar to each other, too. They are featured by a very well-pronounced linear region that must be associated with the onset of strong phonon-assisted absorption. However, this region is preceded from the lower-energy side by the region of a lower slope that looks the same in all four compounds. The difference in the Kubelka–Munk function behavior in this region is mainly due to the contribution of the  $f$ - $f$  transitions of Ln ions that are the fingerprints of the corresponding ions, the presence of such a lower-slope region is often assigned to the presence of crystalline impurities in the structure of the crystals under study. However, Table 8 shows that the overall fraction of impurities is very moderate and ranges from 1.4% in the case of Tm-selenide to 5% in the case of Dy-selenide; that is, the impurity content varies by a factor of six, while the lower-slope region looks the same in height in all crystals. Thus, it is highly likely that the lower-slope region in the Kubelka–Munk function is not due to impurities but is related to the intrinsic properties of the crystals under study. Therefore, to quantify the described behavior of the Kubelka–Munk function, we introduced two indirect bandgaps for every crystal (see Table 8).

**Table 8.** Bandgaps in  $SrLnCuSe_3$  crystals.

$SrLnCuSe_3$	ST	SG	Direct Bandgap, (eV)	Larger Indirect Bandgap, (eV)	Lower Indirect Bandgap, (eV)	Impurity Content (mol. %)
$SrDyCuSe_3$	$Eu_2CuS_3$	$Pnma$	2.14	1.41	0.634	2.3- $SrDySe_2$ 2.7- $Dy_2Si_2O_7$
$SrHoCuSe_3$			2.22	1.45	0.81	4.1- $Ho_2SeO_2$ 1.4- $SrHoSe_2$
$SrErCuSe_3$	$KZrCuS_3$	$Cmcm$	2.3	1.94	1.17	1.1- $SrErSe_2$ 2.6- $Er_2Si_2O_7$
$SrTmCuSe_3$			2.33	2.0	1.19	1.4- $Tm_2SeO_2$

A possible explanation for this lower-slope region in the Kubelka–Munk function and the existence of two bandgaps can be found in the recent study of a  $GdSF$  crystal [34].

Two bandgaps were detected in the Kubelka–Munk function for the indirect bandgap of GdSF; the *ab initio* DFT calculations showed that the existence of the lower-energy bandgap is explained by the specific electronic structure of GdSF, or, in more detail, by a formally direct transition to a highly dispersive subband within the conduction band. It was explained that such transition contributes not to the direct but to the indirect bandgap, and it was proved by direct *ab initio* DFT calculations of the absorption coefficient spectrum of GdSF.

Therefore, we can deduce that it is highly likely that the lower indirect bandgap observed in SrLnCuSe<sub>3</sub> must be explained by the presence of highly dispersive subbands in the electronic structure of the crystals under study via the mechanism explained in [34]. To check the applicability of such an assumption for the crystal structure of SrLnCuSe<sub>3</sub>, we conducted *ab initio* DFT calculations of the electronic structure of the SrTmCuSe<sub>3</sub> crystal. An example of the electronic structure obtained via these calculations is presented in Figure S4 of the Supplementary Materials. Indeed, the calculations show the existence of highly dispersive bands not only at the bottom of conduction bands but at the top of the valence band as well. These bands may be responsible for the formation of the two indirect bandgaps detected in our experimental studies.

The measured bandgap values are presented in Table 8. The bandgap of Ln-containing chalcogenides must be considered dependent on the number of *f* electrons rather than on the ionic radius of Ln. All three values of the bandgaps for all four crystals under study are governed by the well-known law: for the middle of the Ln sequence in the Periodic Table, the bandgap value of quaternary chalcogenides grows with the increase in the number of *f* electrons due to the shift of the energy position of Ln-originating subbands with respect to the overall electronic band structure of a crystal.

### 3.4. Raman Spectrometry

Raman spectra of SrHoCuSe<sub>3</sub> and SrErCuSe<sub>3</sub> are presented in Figure 5. Both spectra contain intense peaks in the range 60–75 cm<sup>-1</sup> as well as pronounced peaks in the range 130–180 cm<sup>-1</sup>. These features are generally similar to, e.g., Raman spectra calculated for EuTbCuSe<sub>3</sub> (SG *Pnma*) and EuTmCuSe<sub>3</sub> (SG *Cmcm*) [5], despite the difference in Sr and Eu atomic weights. The spectrum of SrHoCuSe<sub>3</sub>, in contrast to that of SrErCuSe<sub>3</sub>, contains an intense band at ~20 cm<sup>-1</sup> and a weak band at 44 cm<sup>-1</sup>. The obtained Raman scattering data confirm that the structures of SrHoCuSe<sub>3</sub> and SrErCuSe<sub>3</sub> are characterized by the *Pnma* and *Cmcm* space groups, respectively.

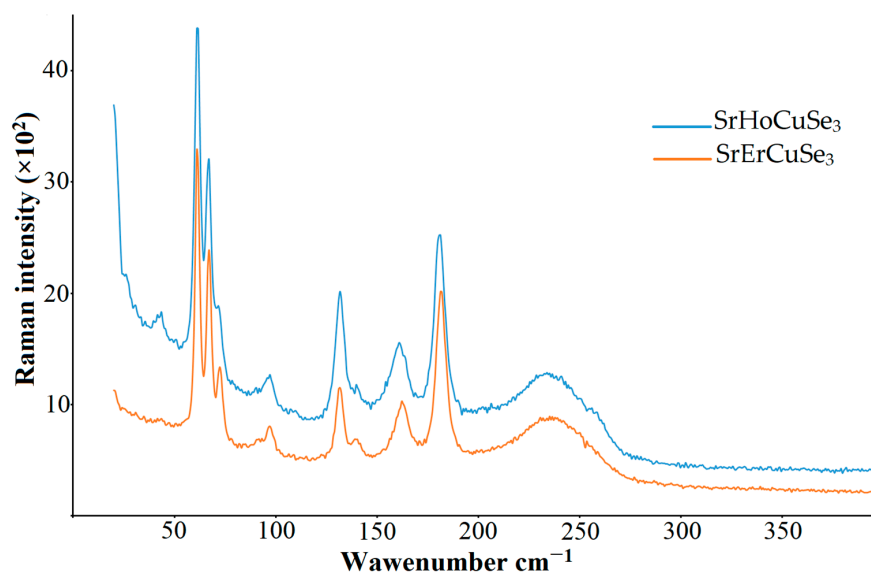


Figure 5. Experimental Raman spectra for SrHoCuSe<sub>3</sub> and SrErCuSe<sub>3</sub>.

### 3.5. Thermal Properties

The DSC measurements showed that the polycrystalline SrLnCuSe<sub>3</sub> samples exhibit thermal effects and undergo incongruent melting leading to the formation of liquid and solid phases (Table 9, Figure 6). The thermal effects exhibited by SrHoCuSe<sub>3</sub> and SrTmCuSe<sub>3</sub> at 1530–1580 K and 1550–1625 K, respectively, are most likely caused by polymorphic transitions. The endothermic peaks of these effects (heating) have pronounced linear segments that are characteristic of phase transformations and correspond to invariant phase equilibria [35]. The peaks of exothermic effects on the DSC cooling dependences appear at approximately the same temperatures. The enthalpies of phase transformations have somewhat smaller values, which is consistent with the decrease in the content of SrLnCuSe<sub>3</sub> phases in the samples after the phases are crystallized from the melt as a result of a peritectic reaction [4].

**Table 9.** Temperatures and enthalpies of the melting and polymorphic transitions of SrLnCuSe<sub>3</sub> (Ln = Dy, Ho, Er, Tm).

Compound	Phase Equilibria					
	$\alpha \rightleftharpoons \beta$		$\beta \rightleftharpoons \gamma$		Melting	
	T, K	$\Delta H$ , J/g	T, K	$\Delta H$ , J/g	T, K	$\Delta H$ , J/g
SrDyCuSe <sub>3</sub>	1550	22.3	1573	3.6	1606	27.2
SrHoCuSe <sub>3</sub>	1555	42.0	1572	7.4	1584	14.2
SrErCuSe <sub>3</sub>	1569	31.2	1599	6.0	1634	38.1
SrTmCuSe <sub>3</sub>	1578	74.9	1600	14.8	1620	-

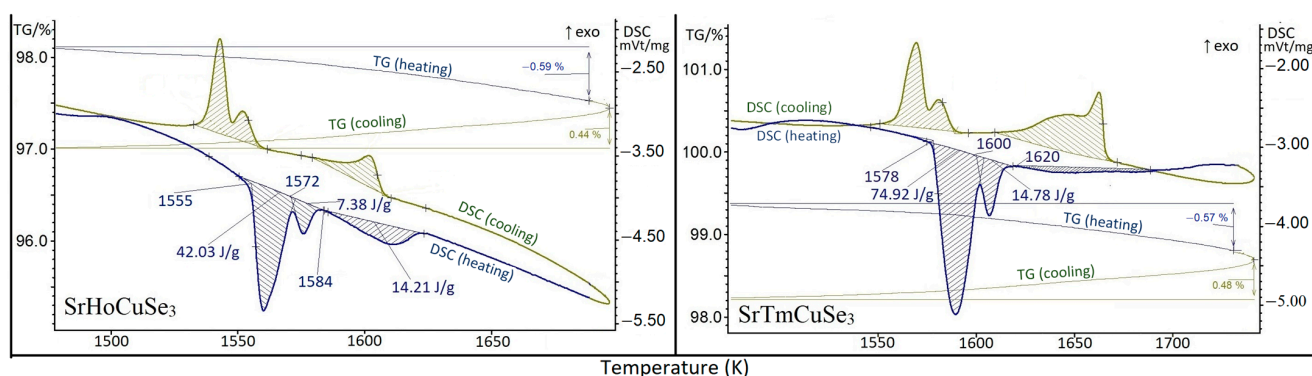


**Figure 6.** DSC/TG/t dependence of “Netzsch” Jupiter F3 for samples of SrHoCuSe<sub>3</sub> and SrTmCuSe<sub>3</sub> (the samples were in open crucibles).

The appearance of the peaks of thermal effects during heating and cooling allows for classifying these phase transformations as “fast”, e.g., like those in Cu<sub>2-x</sub>Se [36]. The samples of SrLnCuSe<sub>3</sub> phases were cooled immediately after reaching the temperatures when the peaks of the first and second phase transformations appeared. The ampoules with the samples were placed into an aqueous salt solution immediately after removing them from the muffle. The phase composition of the samples did not change. The content of SrLnCuSe<sub>3</sub> phases exceeded 95%; the same impurities were present in the sample.

The peaks of the thermal effects of the incongruent melting of the SrLnCuSe<sub>3</sub> samples also have linear segments, but the decomposition occurs in wide temperature ranges ( $\Delta T$ ). The cooling curves of the SrLnCuSe<sub>3</sub> samples contain double peaks of exothermic effects (Figure 6 and Figure S5 in the Supplementary Materials). The first one occurs in a narrow temperature range and is most likely caused by the simultaneous crystallization of SrSe and SrLnCuSe<sub>3</sub> phases from the melt. The second weaker exothermic effect is related to the solid-phase formation of the polycrystalline phases of the system’s components. Above

1450–1500 K, the TG dependence shows some slight deviation. The phase transformations and the incongruent phase melting cause no jumps in the sample weight changes (Figure 6).

The presence of phases was recorded for cooled samples. The phase composition of samples  $\text{SrHoCuSe}_3$  (Figure 7) and  $\text{SrTmCuSe}_3$  (Figure S6 in the Supplementary Materials), which were heated above 1750 K and then cooled, was determined by the SEM method. The samples did not melt completely, but their surface partially did. The samples were formed by  $\text{SrHoCuSe}_3$  (70 mol.%) and  $\text{SrTmCuSe}_3$  (80 mol.%) phases and by solid solutions of metal selenides. The SrSe solid solution phase occurs in the form of isolated oval grains uniformly distributed over the sample volume. The phases of  $\text{Cu}_{2-x}\text{Se}$  and  $\text{Ln}_2\text{Se}_3$  solid solutions have the shape of strips between the grains of other phases or adopt the shape of bulk polyhedral grains. The shape and relative arrangement of the grains indicate that  $\text{SrLnCuSe}_3$  melts incongruently according to the equation:

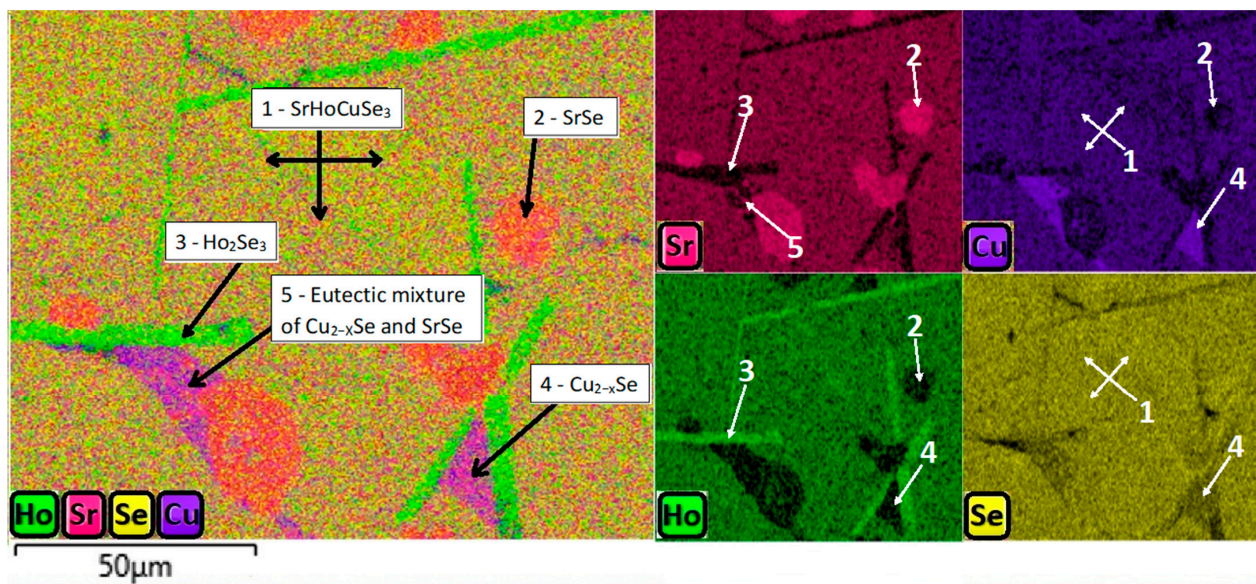


**Figure 7.** SEM/EDS maps of the elemental distribution on the surface of the  $\text{SrHoCuSe}_3$  sample that was cooled after the DSC measurements (1800 K).

All the studied quaternary  $\text{A}^{\text{II}}\text{LnCuSe}_3$  compounds of the yttrium subgroup are characterized by a similar equation of incongruent decomposition [4].

In order to establish the elemental composition of the samples, SEM analysis was carried out on thin sections of annealed samples of  $\text{SrLnCuSe}_3$  ( $\text{Ln} = \text{Dy}, \text{Ho}, \text{Er}, \text{Tm}$ ). According to the results of the analysis, the chemical elements are uniformly distributed over the sample (Table 10). The constituent element ratio, within the limits of determination errors, is consistent with the nominal composition of the sample.

**Table 10.** Theoretical (A) and experimental (B) (according to the SEM data) contents of the chemical elements in the  $\text{SrLnCuSe}_3$  ( $\text{Ln} = \text{Dy}, \text{Ho}, \text{Er}, \text{Tm}$ ) samples.

Compound	Sr (mass %)		Ln (mass %)		Cu (mass %)		Se (mass %)	
	A	B	A	B	A	B	A	B
$\text{SrDyCuSe}_3$	15.91	$15.3 \pm 0.3$	29.52	$31.4 \pm 0.4$	11.53	$10.5 \pm 0.5$	43.0	$42.8 \pm 0.5$
$\text{SrHoCuSe}_3$	15.84	$14.9 \pm 0.5$	29.82	$30.5 \pm 0.2$	11.48	$12.3 \pm 0.2$	42.81	$42.3 \pm 0.3$
$\text{SrErCuSe}_3$	15.78	$15.2 \pm 0.5$	30.13	$31.9 \pm 0.5$	11.44	$11.0 \pm 0.6$	42.63	$41.8 \pm 0.4$
$\text{SrTmCuSe}_3$	15.73	$16.6 \pm 0.4$	30.32	$29.0 \pm 0.2$	11.40	$11.5 \pm 0.2$	42.50	$42.8 \pm 0.4$

#### 4. Conclusions

In the present work, new complex selenides with the participation of transition metals were obtained and their crystal structure was established by single-crystal and powder XRD diffraction and by Raman spectroscopy methods. The compounds are paramagnetic over the entire range of the temperatures studied. Copper ions do not contribute to the magnetic state; therefore, the state is determined by the electronic state of lanthanide ions and agrees well with their theoretical values. A slight discrepancy with the theoretical values in the case of compounds containing  $\text{Dy}^{3+}$ ,  $\text{Ho}^{3+}$ , and  $\text{Tm}^{3+}$  ions is explained by an increase in the relative contribution of the crystal-field splitting of the multiplets of the ground states of these ions. All the compounds show a direct bandgap in the range of 2.14–2.31 eV. The presence of bandgaps in all the studied compounds is explained by the presence of optical transitions to highly dispersive subbands in the conduction band. The studied compounds are stable up to 1273 K; therefore, they can be obtained in the form of technical ceramics of a required shape and can be used as potential spintronics and thermoelectric materials and as p- and n-type semiconductors, which is the subject of further research.

**Supplementary Materials:** The following supporting information can be downloaded at: <https://www.mdpi.com/article/10.3390/magnetochemistry9080194/s1>. Table S1: Main parameters of processing and refinement of the  $\text{SrTmCuSe}_3$  samples. Table S2: Fractional atomic coordinates and isotropic displacement parameters ( $\text{\AA}^2$ ) of  $\text{SrTmCuSe}_3$ . Table S3: Main bond lengths ( $\text{\AA}$ ) of  $\text{SrTmCuSe}_3$ . Figure S1: Polyhedral structure of  $\text{SrTmCuSe}_3$ . Figure S2: Kubelka-Munk Functions for determination of direct bandgaps in  $\text{SrLnCuSe}_3$  crystals. Figure S3: UV-vis-NIR diffuse reflectance spectra of quaternary rare earth selenides. Figure S4: *Ab initio* DFT calculated band structure of  $\text{SrTmCuSe}_3$  crystal. Figure S5: DSC/t dependences of “SETARAM” SETSYS Evolution for samples  $\text{SrDyCuSe}_3$ ,  $\text{SrErCuSe}_3$ . Figure S6: SEM/EDS maps of elemental distribution on the surface  $\text{SrTmCuSe}_3$  sample that were cooled after the DSC measurements.

**Author Contributions:** Conceptualization, N.G.N., Y.G.D. and O.V.A.; methodology, O.V.A.; formal analysis, N.N.H. and N.G.N.; investigation, N.N.H., A.N.L., N.V.K., A.S.A., A.S.O., M.S.M., I.V.P. and A.D.Z.; data curation, N.N.H., N.G.N. and I.O.Y.; writing—original draft preparation, A.N.L., A.S.A. and O.V.A.; writing—review and editing, N.N.H., N.G.N., A.N.L., I.O.Y., Y.G.D. and A.D.Z.; visualization, N.N.H., N.V.K. and M.S.M.; supervision, O.V.A. All authors have read and agreed to the published version of the manuscript.

**Funding:** The study was funded by the Russian Science Foundation, project No. 23-23-00488.

**Institutional Review Board Statement:** Not applicable.

**Informed Consent Statement:** Not applicable.

**Data Availability Statement:** The data is available from the authors upon reasonable request.

**Acknowledgments:** Spectrophotometric studies were carried out using the equipment in the Center for Collective Use “Rational Nature Management and Physicochemical Research” of Tyumen State University.

**Conflicts of Interest:** The authors declare no conflict of interest.

#### References

1. Strobel, S.; Schleid, T. Three Structure Types for Strontium Copper (I) Lanthanide(III) Selenides  $\text{SrCuMSe}_3$  ( $M = \text{La, Gd, Lu}$ ). *J. Alloys Compd.* **2006**, *418*, 80–85. [[CrossRef](#)]
2. Strobel, S.; Schleid, T. Quaternary strontium copper (I) lanthanoid (III) selenides with cerium and praseodymium:  $\text{SrCuCeSe}_3$  and  $\text{SrCuPrSe}_3$ , unequal brother and sister. *Z. Naturforsch.* **2004**, *59*, 985–991. [[CrossRef](#)]
3. Shahid, O.; Yadav, S.; Maity, D.; Deepa, M.; Niranjana, M.K.; Prakash, J. Synthesis, Crystal Structure, DFT, and Photovoltaic Studies of  $\text{BaCeCuS}_3$ . *New J. Chem.* **2023**, *47*, 5378–5389. [[CrossRef](#)]
4. Andreev, O.V.; Atuchin, V.V.; Aleksandrovsky, A.S.; Denisenko, Y.G.; Zakharov, B.A.; Tyutyunnik, A.P.; Habibullayev, N.N.; Velikanov, D.A.; Ulybin, D.A.; Shpindyuk, D.D. Synthesis, Structure, and Properties of  $\text{EuLnCuSe}_3$  ( $\text{Ln} = \text{Nd, Sm, Gd, Er}$ ). *Crystals* **2022**, *12*, 17. [[CrossRef](#)]

5. Grigoriev, M.V.; Solovyov, L.A.; Ruseikina, A.V.; Aleksandrovsky, A.S.; Chernyshev, V.A.; Velikanov, D.A.; Garmonov, A.A.; Molokeev, M.S.; Oreshonkov, A.S.; Shestakov, N.P.; et al. Quaternary Selenides  $\text{EuLnCuSe}_3$ : Synthesis, Structures, Properties and In Silico Studies. *Int. J. Mol. Sci.* **2022**, *23*, 1503. [[CrossRef](#)]
6. Gulay, L.D.; Kaczorowski, D.; Pietraszko, A. Crystal structure and magnetic properties of  $\text{YbCuPbSe}_3$ . *J. Alloys Compd.* **2006**, *413*, 26–28. [[CrossRef](#)]
7. Ishtiyak, M.; Jana, S.; Karthikeyan, R.; Ramesh, M.; Tripathy, B.; Malladi, S.K.; Niranjana, M.K.; Prakash, J. Syntheses of Five New Layered Quaternary Chalcogenides  $\text{SrScCuSe}_3$ ,  $\text{SrScCuTe}_3$ ,  $\text{BaScCuSe}_3$ ,  $\text{BaScCuTe}_3$ , and  $\text{BaScAgTe}_3$ : Crystal Structures, Thermoelectric Properties, and Electronic Structures. *Inorg. Chem. Front.* **2021**, *8*, 4086–4101. [[CrossRef](#)]
8. Mitchell, K.; Huang, F.Q.; McFarland, A.D.; Haynes, C.L.; Somers, R.C.; Van Duyn, R.P.; Ibers, J.A. The  $\text{CsLnMSe}_3$  semiconductors (Ln = rare-earth element, Y; M = Zn, Cd, Hg). *Inorg. Chem.* **2003**, *42*, 4109–4116. [[CrossRef](#)]
9. Wakeshima, M.; Furuuchi, F.; Hinatsu, Y. Crystal Structures and Magnetic Properties of Novel Rare-Earth Copper Sulfides,  $\text{EuRCuS}_3$  (R = Y, Gd–Lu). *J. Phys. Condens. Matter* **2004**, *16*, 5503–5518. [[CrossRef](#)]
10. Furuuchi, F.; Wakeshima, M.; Hinatsu, Y. Magnetic Properties and 151Eu Mössbauer Effects of Mixed Valence Europium Copper Sulfide,  $\text{Eu}_2\text{CuS}_3$ . *J. Solid State Chem.* **2004**, *177*, 3853–3858. [[CrossRef](#)]
11. van den Eckhout, K.; Smet, P.F.; Poelman, D. Persistent luminescence in  $\text{Eu}^{2+}$ -doped compounds: A review. *Materials* **2010**, *3*, 2536–2566. [[CrossRef](#)]
12. Ruseikina, A.V.; Grigoriev, M.V.; Solovyov, L.A.; Chernyshev, V.A.; Aleksandrovsky, A.S.; Krylov, A.S.; Krylova, S.N.; Shestakov, N.P.; Velikanov, D.A.; Garmonov, A.A.; et al. A Challenge toward Novel Quaternary Sulfides  $\text{SrLnCuS}_3$  (Ln = La, Nd, Tm): Unraveling Synthetic Pathways, Structures and Properties. *Int. J. Mol. Sci.* **2022**, *23*, 12438. [[CrossRef](#)]
13. Acosta-Silva, Y.D.J.; Godínez, L.A.; Toledano-Ayala, M.; Lozada-Morales, R.; Zelaya-Angel, O.; Méndez-López, A. Study of the Effects of Er Doping on the Physical Properties of CdSe Thin Films. *Magnetochemistry* **2023**, *9*, 107. [[CrossRef](#)]
14. Belkhir, L.; Le Guennic, B.; Boucekkine, A. DFT Investigations of the Magnetic Properties of Actinide Complexes. *Magnetochemistry* **2019**, *5*, 15. [[CrossRef](#)]
15. Kroumova, E.; Aroyo, M.I.; Perez-Mato, J.M.; Kirov, A.; Capillas, C.; Ivantchev, S.; Wondraschek, H. Bilbao Crystallographic Server: Useful databases and tools for phase-transition studies. *Phase Transit.* **2003**, *76*, 155–170. [[CrossRef](#)]
16. Azarapin, N.O.; Aleksandrovsky, A.S.; Atuchin, V.V.; Gavrilova, T.A.; Krylov, A.S.; Molokeev, M.S.; Mukherjee, S.; Oreshonkov, A.S.; Andreev, O.V. Synthesis, structural and spectroscopic properties of orthorhombic compounds  $\text{BaLnCuS}_3$  (Ln = Pr, Sm). *J. Alloys Compd.* **2019**, *832*, 153134. [[CrossRef](#)]
17. Ruseikina, A.V.; Andreev, O.V.; Galenko, E.O.; Koltsov, S.I. Trends in Thermodynamic Parameters of Phase Transitions of Lanthanide Sulfides  $\text{SrLnCuS}_3$  (Ln = La–Lu). *J. Therm. Anal. Calorim.* **2016**, *128*, 993–999. [[CrossRef](#)]
18. Shtykova, M.A.; Molokeev, M.S.; Zakharov, B.A.; Selezneva, N.V.; Aleksandrovsky, A.S.; Bubnova, R.S.; Kamaev, D.N.; Gubin, A.A.; Habibullayev, N.N.; Matigorov, A.V.; et al. Structure and Properties of Phases in the  $\text{Cu}_{2-x}\text{Se-Sb}_2\text{Se}_3$  System. The  $\text{Cu}_{2-x}\text{Se-Sb}_2\text{Se}_3$  Phase Diagram. *J. Alloys Compd.* **2022**, *906*, 164384. [[CrossRef](#)]
19. Strobel, S.; Schleid, T. Quaternäre Cäsium-Kupfer(I)-Lanthanoid(III)-Selenide vom Typ  $\text{CsCu}_3\text{M}_2\text{Se}_5$  (M = Sm, Gd–Lu). *Z. Für Anorg. Und Allg. Chem.* **2004**, *630*, 706–711. [[CrossRef](#)]
20. Lee, H.N.; Zakharov, D.N.; Senz, S.; Pignolet, A.; Hesse, D. Epitaxial Growth of Ferroelectric  $\text{SrBi}_2\text{Ta}_2\text{O}_9$  Thin Films of Mixed (100) and (116) Orientation on  $\text{SrLaGaO}_4(110)$ . *Appl. Phys. Lett.* **2001**, *79*, 2961–2963. [[CrossRef](#)]
21. Bruker AXS TOPAS V4: General Profile And Structure Analysis Software for Powder Diffraction Data—User’s Manual; Bruker AXS: Karlsruhe, Germany, 2008.
22. Pomelova, T.A.; Delacotte, C.; Kuratieva, N.V.; Lemoine, P.; Cordier, S.; Park, S.; Guizouarn, T.; Pelletier, V.; Gautier, R.; Naumov, N.G.  $\text{Cs}_2\text{Ln}_3\text{CuS}_8$  (Ln = La–Nd, Sm–Tb): Synthesis, Crystal Structure, and Magnetic and Optical Properties. *Inorg. Chem.* **2023**, *62*, 6586–6597. [[CrossRef](#)]
23. Park, S.C.; Kuratieva, N.V.; Pomelova, T.A.; Naumov, N.G. Synthesis and Crystal Structure of  $\text{CsLnZnS}_3$  (Ln = Gd, Dy). *J. Struct. Chem.* **2022**, *63*, 868–873. [[CrossRef](#)]
24. Bruker. APEX2 (Version 2012.2-0), SAINT (Version 8.18c), and SADABS (Version 2008/1); Bruker AXS Inc.: Madison, WI, USA, 2012.
25. Sheldrick, G.M. SHELXT—Integrated Space-Group and Crystal-Structure Determination. *Acta Crystallogr. A Found Adv.* **2015**, *71*, 3–8. [[CrossRef](#)]
26. Sheldrick, G.M. A Short History of SHELX. *Acta Cryst. A* **2008**, *64*, 112–122. [[CrossRef](#)]
27. Fomenko, I.S.; Afewerki, M.; Gongola, M.I.; Vasilyev, E.S.; Shul’pina, L.S.; Ikonnikov, N.S.; Shul’pin, G.B.; Samsonenko, D.G.; Yanshole, V.V.; Nadolinny, V.A.; et al. Novel Copper(II) Complexes with Dipinodiazfluorene Ligands: Synthesis, Structure, Magnetic and Catalytic Properties. *Molecules* **2022**, *27*, 4072. [[CrossRef](#)]
28. Flakina, A.M.; Zhilyaeva, E.I.; Shilov, G.V.; Faraonov, M.A.; Torunova, S.A.; Konarev, D.V. Layered Organic Conductors Based on BEDT-TTF and Ho, Dy, Tb Chlorides. *Magnetochemistry* **2022**, *8*, 142. [[CrossRef](#)]
29. NETZSCH Proteus 6. Thermic Analyses—User’s and Software Manuals; NETZSCH: Selb, Germany, 2012.
30. Shtykova, M.A.; Vorob’eva, V.P.; Fedorov, P.P.; Molokeev, M.S.; Aleksandrovsky, A.S.; Elyshev, A.V.; Palamarchuk, I.V.; Yurev, I.O.; Ivanov, A.V.; Habibullayev, N.N.; et al. Features of phase equilibria and properties of phases in the Sb–Sm–Se system. *J. Solid State Chem.* **2022**, *316*, 123573. [[CrossRef](#)]
31. Shepilov, M.P.; Dymshits, O.S.; Zhilin, A.A.; Zapalova, S.S. On the Measurements of Scattering Coefficient of Nanostructured Glass-Ceramics by a Serial Spectrophotometer. *Measurement* **2017**, *95*, 306–316. [[CrossRef](#)]

32. Lavrent'ev, Y.G.; Karmanov, N.S.; Usova, L.V. Electron Probe Microanalysis of Minerals: Microanalyzer or Scanning Electron Microscope. *Russ. Geol. Geophys.* **2015**, *56*, 1154–1161. [[CrossRef](#)]
33. Zvezdin, A.K.; Matveev, V.M.; Mukhin, A.A.; Popov, A.I. *Rare Earth Ions in Magnetically Ordered Crystals*; Nauka: Moscow, Russia, 1985.
34. Abulkhaev, M.U.; Molokeev, M.S.; Oreshonkov, A.S.; Aleksandrovsky, A.S.; Kertman, A.V.; Kamaev, D.N.; Trofimova, O.V.; Elyshev, A.V.; Andreev, O.V. Properties of GdSF and phase diagram of the GdF<sub>3</sub>-Gd<sub>2</sub>S<sub>3</sub> system. *J. Solid State Chem.* **2023**, *322*, 123991. [[CrossRef](#)]
35. Andreev, P.O.; Polkovnikov, A.A.; Denisenko, Y.G.; Andreev, O.V.; Burkhanova, T.M.; Bobylevb, A.N.; Pimneva, L.A. Temperatures and Enthalpies of Melting of Ln<sub>2</sub>S<sub>3</sub> (Ln = Gd, Tb, Dy, Ho, Er, Tm, Yb, and Lu) Compounds. *J. Therm. Anal. Calorim.* **2018**, *131*, 1545–1551. [[CrossRef](#)]
36. Thompson, J.O.; Anderson, M.D.; Ngai, T.; Allen, T.; Johnson, D.C. Nucleation and growth kinetics of co-deposited copper and selenium precursors to form metastable copper selenides. *J. Alloys Compd.* **2011**, *509*, 9631–9637. [[CrossRef](#)]

**Disclaimer/Publisher's Note:** The statements, opinions and data contained in all publications are solely those of the individual author(s) and contributor(s) and not of MDPI and/or the editor(s). MDPI and/or the editor(s) disclaim responsibility for any injury to people or property resulting from any ideas, methods, instructions or products referred to in the content.